Supplementary Information

Solution-Processable and Photo-Curable System for Low-cost and Scalable Transient Electronics

*Won Bae Han[1,2,13], Sungkeun Han[1,13], Taekyung Kim[3,4,13], Tae-Min Jang[1,5], Gwan-Jin Ko[1,6], Jaesoon Joo[3], Taewoo Kim[3], Kyu-Sung Lee[4,7], Young-Min Shon[4,8], Eunkyoung Park[9], Venkata Ramesh Naganaboina[10], and Suk-Won Hwang[1,11,12,]**

[1] KU-KIST Graduate School of Converging Science and Technology, Korea University, Seoul 02841, Republic of Korea.

[2] School of Electronic Engineering, Kyonggi University, Suwon, Gyeonggi-do 16227, Republic of Korea.

[3] Biomedical Engineering Research Center, Samsung Medical Center, Seoul 06351, Republic of Korea

[4] Department of Medical Device Management and Research, SAIHST, Sungkyunkwan University, Seoul 06351, Republic of Korea

[5] Semiconductor R&D Center, Samsung Electronics, Gyeonggi-Do 18448, Republic of Korea

[6] Display Research Center, Samsung Display, Gyeonggi-Do 17113, Republic of Korea

[7] Department of Urology, Samsung Medical Center, Sungkyunkwan University School of Medicine, Seoul 06351, Republic of Korea

[8] Department of Neurology, Samsung Medical Center, Sungkyunkwan University School of Medicine, Seoul 06351, Republic of Korea

[9] Department of Biomedical Engineering, Soonchunhyang University, Asan 31538, Republic of Korea

[10] Department of Electronics and Communication Engineering, Amrita School of Engineering, Amrita Vishwa Vidyapeetham, Amaravati Campus, Andhra Pradesh 522503, India

[11] Center for Biomaterials, Biomedical Research Institute, Korea Institute of Science and Technology (KIST), Seoul 02792, Republic of Korea

[12] Department of Integrative Energy Engineering, Korea University, Seoul 02841, Republic of Korea

[13] These authors contributed equally: Won Bae Han, Sungkeun Han, Taekyung Kim

* Corresponding author: dupong76@korea.ac.kr

Supplementary Notes

Supplementary Note 1. Mechanical, structural, electrical, and biochemical characterizations

Mechanical tensile test was performed with a universal testing machine (Instron 5900 series, USA) by applying uniaxial strain to a specimen (length: 20 mm, width: 10 mm) at a consistent loading rate of 6 mm/min. Topographical data were acquired using a Dektak XT (Bruker, USA), while surface morphologies were observed with an optical microscope (BX53M, OLYMPUS, Japan). Electrical conductivity was evaluated using a standard four-point probe (CMT-100A, Advanced Instrument Technology, Korea). For dissolution test, UV-PLCL films based on different molecular weight (0.5k, 1k, and 2k) of PLCL-diol were immersed in a phosphate-buffered saline (PBS, Deajungchem, Korea) at varying pH levels (3, 7, and 11) and temperatures (RT, 37 °C, and 50 °C) for 10 weeks. Each film was extracted weekly, rinsed with DI water, dried in a vacuum oven at 50 ºC overnight, and then weighed to determine the weight loss ratio (%).

Supplementary Note 2. Characterization of electronic components

OTFT. Transfer characteristics were assessed using a mechanical probe station (HP 4145B, Hewlett-Packard, USA). The gate voltage (V_G) was swept from 10 to -30 V with a constant drain voltage (V_D) of -1 V. Stable operability under strains was measured by applying strains ranging from 0 to 30 % parallel and perpendicular to the channel direction using a custom-made stretching system. The field effect mobility of OTFT (μ_{FE}) was calculated in linear regime using the equation:

$$I_{DS} = \frac{WC_i}{L}\mu_{FE}(V_G - V_{TH})V_{DS} \qquad (1)$$

$$\mu_{FE} = \frac{L}{WC_iV_{DS}}\left(\frac{\partial I_{DS}}{\partial V_G}\right) \quad (2)$$

where W, L, and C_i represent the width and length of channel, and the capacitance of gate dielectric. The threshold voltage (V_{TH}) was extrapolated by linearly fitting the transfer curves.

Strain sensor. Strain sensor was mounted on a custom-made stretching system, and current-voltage (I-V) characteristics under strains were measured using a source meter (Kiethley 2636b, USA) with LabVIEW software (National Instruments, USA) at a sample rate of 1 kHz.

Temperature sensor/heater. Temperature sensor was positioned on a hotplate, and changes in resistance during heating from ~25 °C to 75 °C were monitored using a source meter. Heating capability was evaluated by applying voltage to the heater using a power supply and observing temperature changes with an infrared (IR) thermal imaging camera (Fluke Ti480 PRO, Fluke, USA).

Pressure sensor. Colored stainless-steel blocks with different weights (~1.0, ~0.6, and ~0.3 g) were placed on a 5x5 array of capacitive pressure sensors. The resulting pressure distribution was recorded by measuring capacitance changes using an LCR meter (IM 3533-10, HIOKI, Japan).

EP sensing probes. For electromyography (EMG) measurements, EP sensing probes for source and reference were located at the center of the flexor carpi radialis on the inner left arm, with a ground probe attached to the inner left wrist. The signal was acquired by repeatedly clenching and opening the left fist three times. According to the lead I of standard limb leads, electrocardiography (ECG) signals were obtained for 30 s by attaching EP probes for source and reference on the inner left and right arms, respectively, with a ground probe on the inner left foot. For comparison, commercial Ag/AgCl probes were placed on similar locations as the EP probes and used to record signals. All signals were amplified by a factor of 1000 using an amplifier (Model 1700 differential AC amplifier, A-M Systems, USA), processed with a bandpass (0.5 - 100 Hz) and notch filters to reduce power line interference, and obtained at a sampling frequency of 1 kHz by a NI DAQ (National instrument, USA). The signals were further processed with the third-order Butterworth bandpass filter (0.1 - 40 Hz) using Matlab (MathWorks, USA).

Supplementary Note 3. Histology and blood analysis

All rats were deeply anesthetized with 2% isoflurane, followed by transcardial perfusion with saline to remove blood. The animals were then decapitated at the 6 mm interaural plane to collect brain tissue along with the overlying skin and skull. The harvested samples were fixed in 4% paraformaldehyde (PFA) at 4 °C for over 24 hours, decalcified in 10% ethylenediaminetetraacetic acid (EDTA) for 4 weeks, embedded in paraffin blocks, and sectioned at a thickness of 4 μm. Immunohistochemistry was performed using antibodies against CD68 (ab125212, Abcam, Cambridge, UK, diluted 1:200) and TNF-α (ab6671, diluted 1:200). Antigen retrieval was carried out using Proteinase K for CD68 and citrate buffer (pH 6.0) for TNF-α. Primary antibody incubation was conducted overnight at 4°C. Stained tissue sections were imaged using the Aperio ScanScope AT2 system (Leica Biosystems, USA). To evaluate blood chemistry, approximately 3 mL of blood was collected from each animal into EDTA-coated gel tubes during immunochemistry sample preparation. Greenvet Laboratory (South Korea) conducted the assays.

Supplementary Note 4. *In vivo* neural recording during toe pinch test

For the toe pinch test, the experimenter manually pinched the rat's toes ten times, and each event marked in the acquisition software. A bandpass filter (1 to 30 Hz) was applied to the ECoG data. Based on event markers, the 500 ms preceding each pinch was defined as the baseline, and the 500 ms following was identified as the toe pinch bin. Signals from each bin were averaged across trials.

Supplementary Note 5. *In vivo* cardiac monitoring and stimulation

To record epicardial ECG signals and perform cardiac pacing, a thoracotomy was conducted to expose the heart. A soft, conformal, transient cardiac electrode array was placed directly onto the epicardial surface and secured using BioGlue, followed by recording epicardial ECG signals. For surface ECG measurement, three commercial electrodes (Red Dot 2239, 3M, USA) were attached to the right foreleg as a negative pole, the left hindleg as a positive pole, and the left foreleg as a ground electrode. Electrical stimulation (biphasic; 400 Hz, 50 μA, 100 μs, 5 s duration) was applied to modulate heart rate while epicardial ECG signals were simultaneously monitored in real-time.

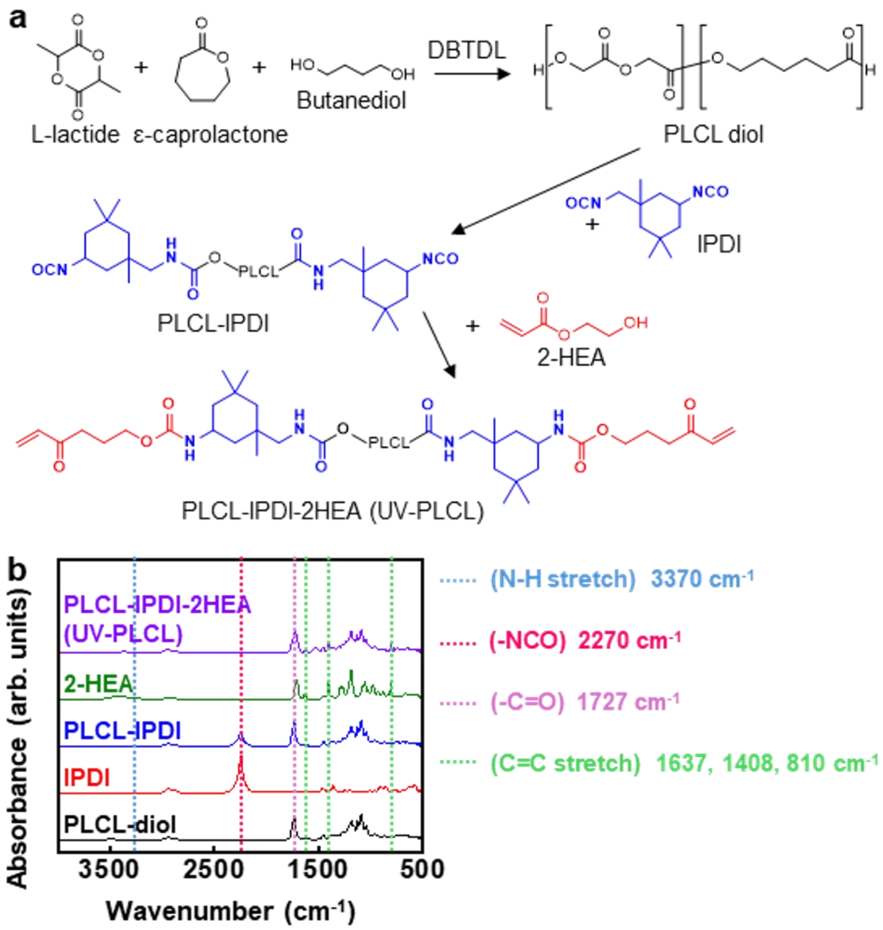

Figure S1. (a) Schematic illustration of the synthetic procedure for UV-PLCL. (b) FT-IR spectra of PLCL-diol, IPDI, PLCL-IPDI, 2-HEA, and the final product, UV-PLCL.

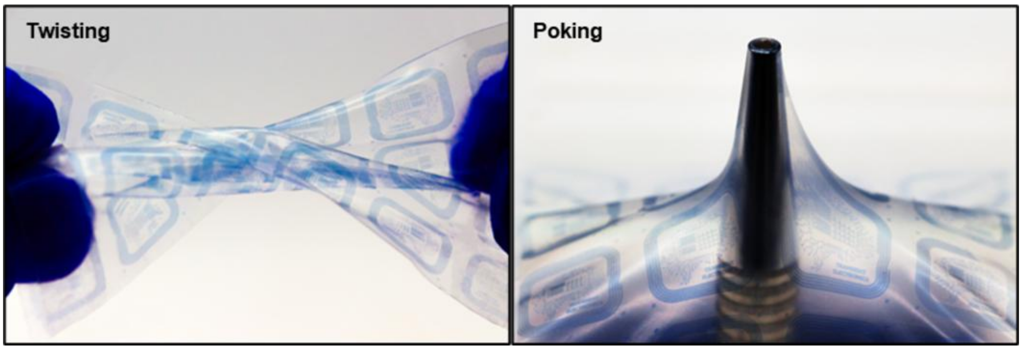

Figure S2. Optical images of a soft, stretchable, wafer-scale transient system under twisting (left) and poking (right).

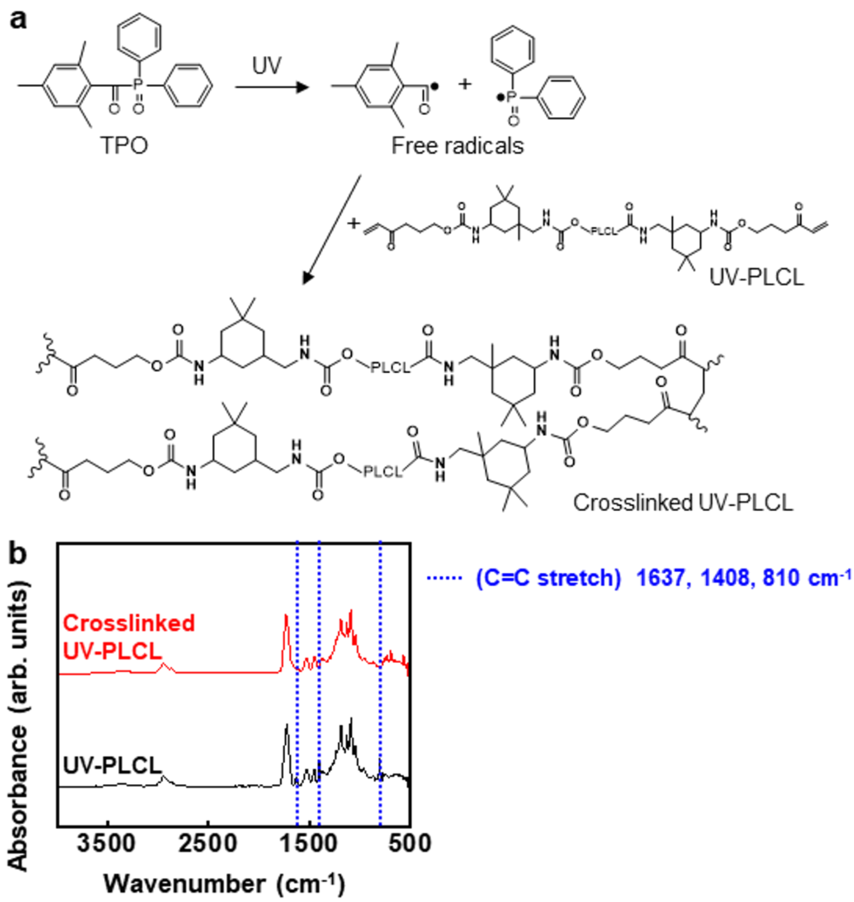

Figure S3. (a) Crosslinking mechanism of UV-PLCL. (b) FT-IR spectra of UV-PLCL before and after crosslinking.

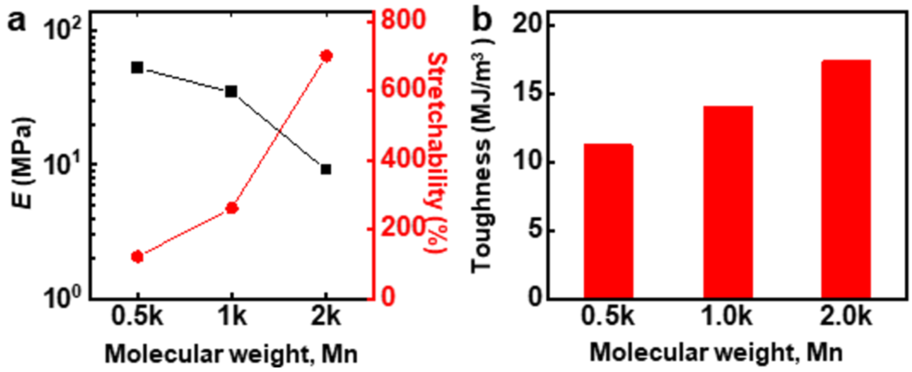

Figure S4. (a) Measured elastic moduli and stretchability, and (b) calculated toughness of insulators (crosslinked UV-PLCL films, 100 μm) synthesized with different molecular weights of PLCL prepolymer.

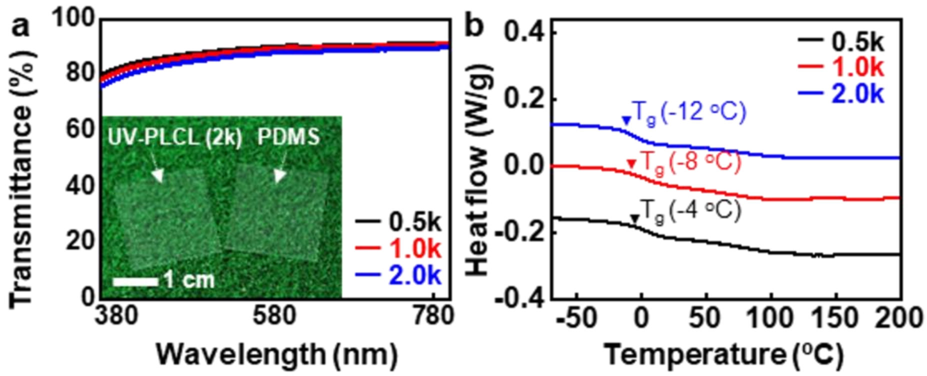

Figure S5. (a) Optical transmittance and (b) DSC spectra of insulators with different molecular weights of PLCL prepolymer. The inset in (a) highlights the high transparency of an insulator film (100 μm-thick) made with 2k PLCL prepolymer, comparable to that of PDMS (10:1).

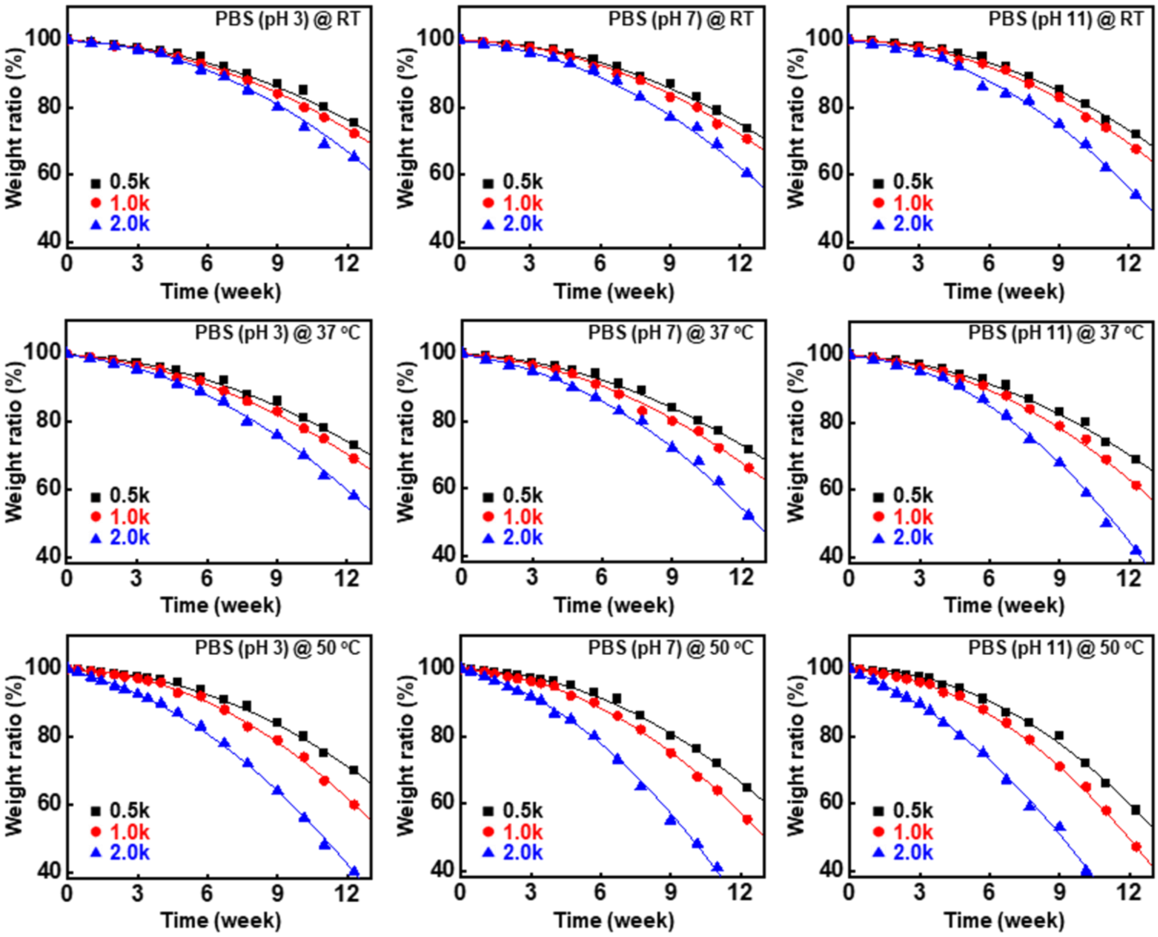

Figure S6. Dissolution behaviors of insulators with varying molecular weights of PLCL prepolymer in PBS under varying pH and temperature conditions.

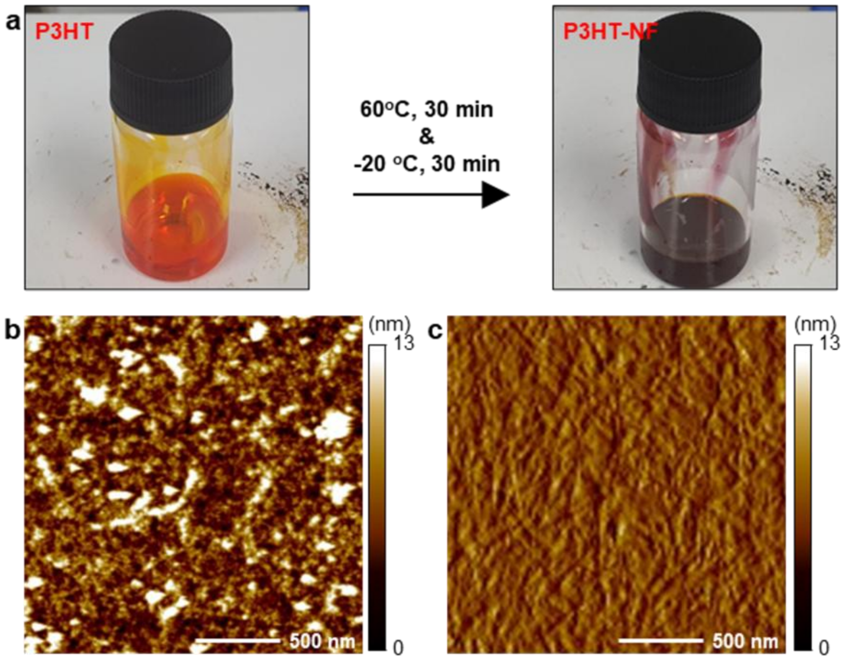

Figure S7. (a) Photographs of P3HT and P3HT-NF solutions. (b,c) Atomic force microscopy (AFM) analysis of the surface morphology of P3HT (b) and P3HT-NF (c) films.

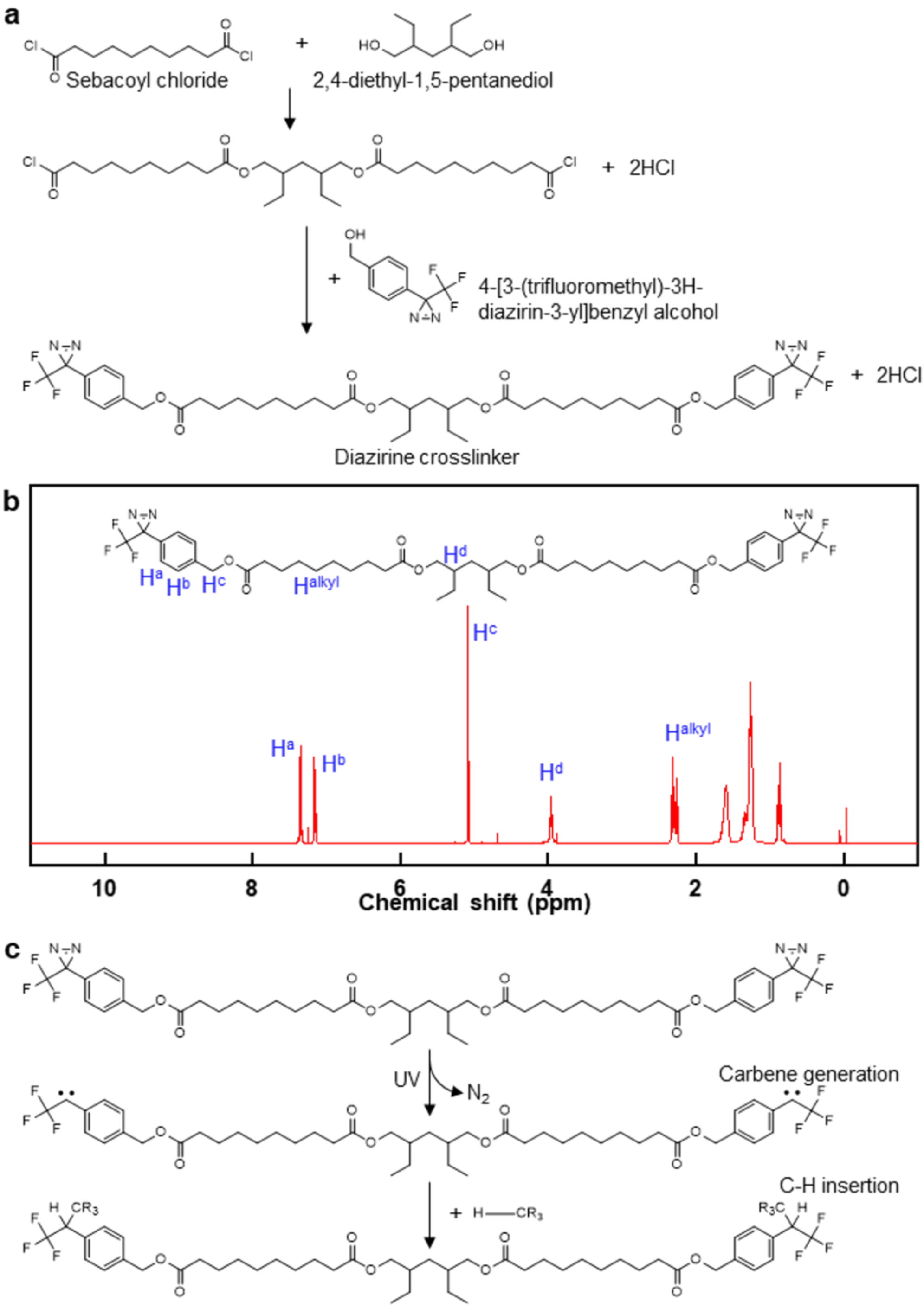

Figure S8. (a) Synthetic scheme of the diazirine crosslinker. (b) NMR spectrum of the synthesized diazirine crosslinker. (c) Crosslinking mechanism via carbene insertion.

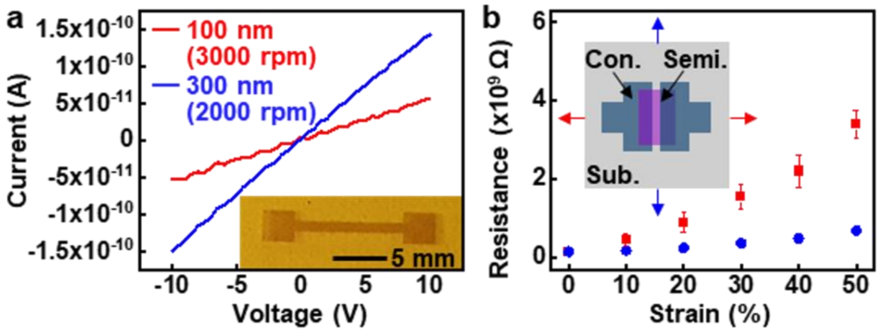

Figure S9. (a) I-V curves of semiconductor patterns with different thicknesses, with a dog-bone-shaped semiconductor pattern in the inset. (b) Resistance changes in a semiconductor layer deposited on conductor pads under horizontal and perpendicular strain, with schematic of the experimental setup in the inset. Data are presented as mean values ± standard deviation. n=5 independent samples.

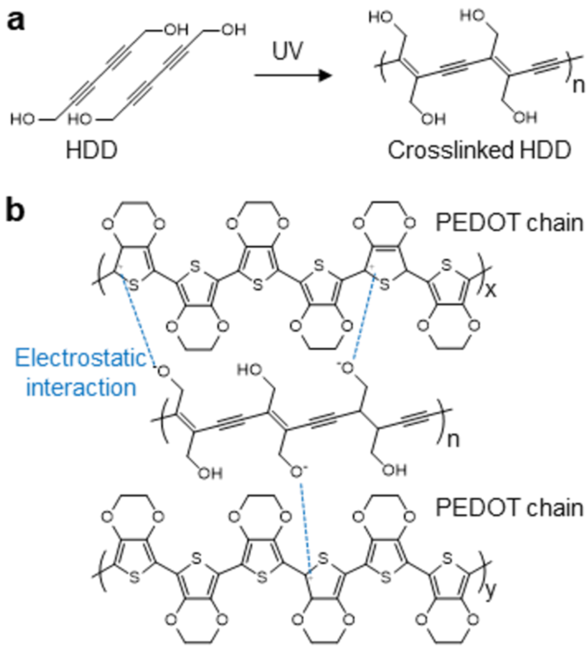

Figure S10. (a) Polymerization mechanism of HDD crosslinkers. (b) Schematic of electrostatic interactions between hydroxyl groups in crosslinked HDD and PEDOT domains in PEDOT:PSS.

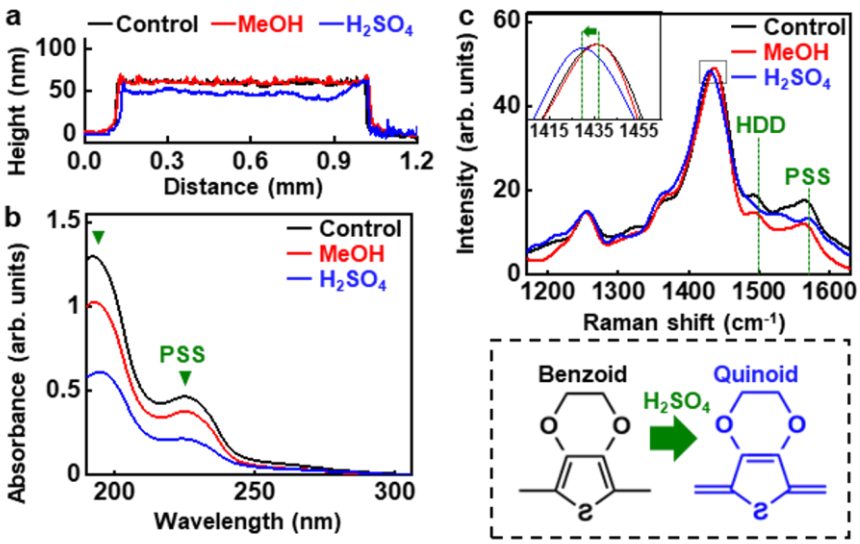

Figure S11. (a) Dektak surface profiles, (b) UV-Vis spectra, and (c) Raman spectra of conductor thin films before and after treatment with methanol (MeOH) and sulfuric acid (H_2SO_4), with an inset (bottom right) illustrating the transformation of PEDOT configuration from benzoid to quinoid structure upon doping with sulfuric acid.

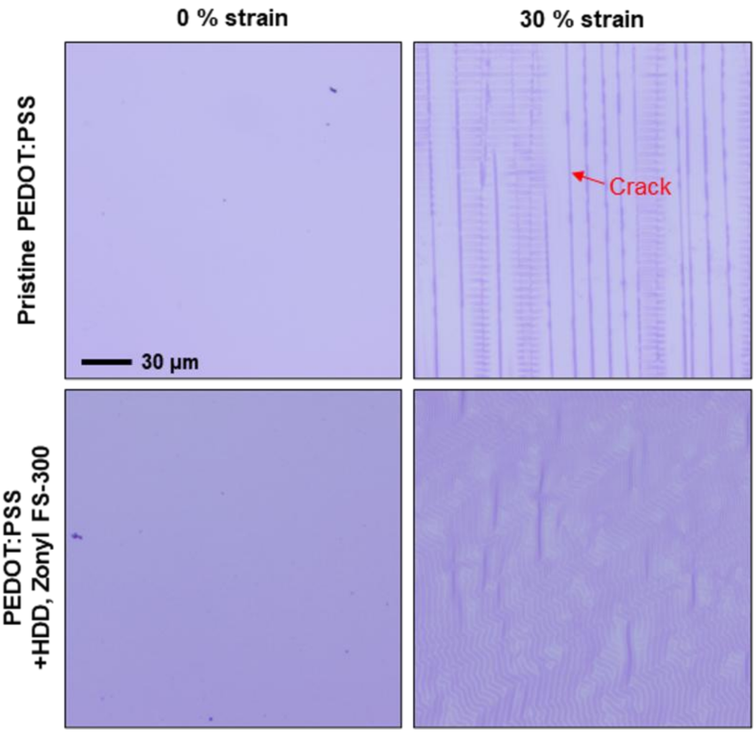

Figure S12. Optical images of pristine PEDOT:PSS and the developed conductor (PEDOT:PSS + HDD + Zonyl FS-300) before (left) and after (right) 1,000 bending cycles (2 mm radius), demonstrating crack suppression by the HDD network and surfactant.

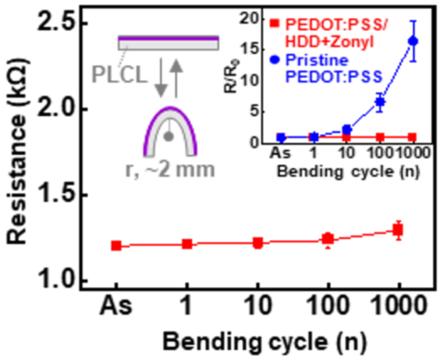

Figure S13. Resistance change of a conductor deposited on a PLCL film under cyclic bending (bending radius, 2 mm) and comparison of strain-dependent electrical performance of pristine PEDOT:PSS and the optimized conductor (10 wt% HDD) in the inset. Data are presented as mean values ± standard deviation. n=5 independent samples.

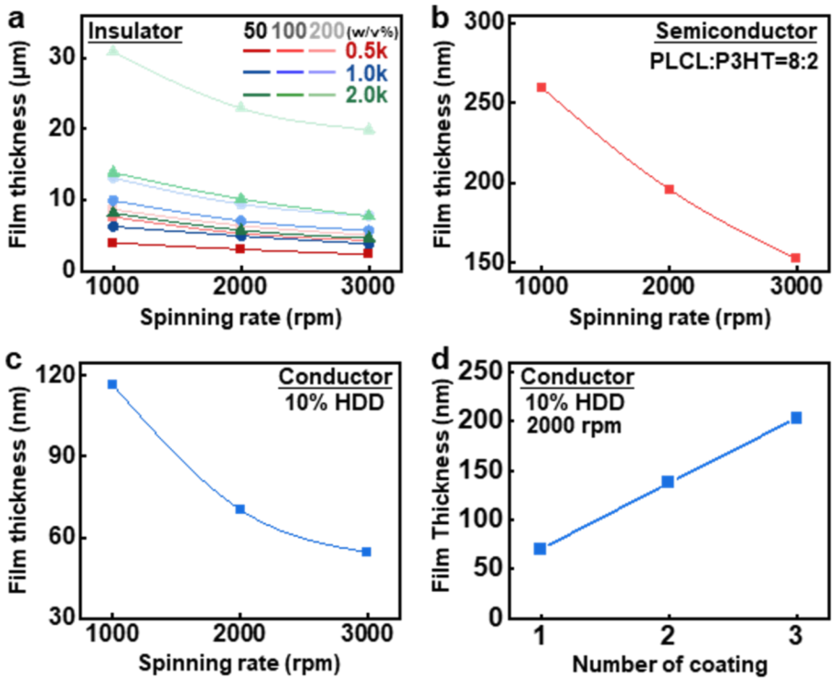

Figure S14. (a-c) Measured film thicknesses of insulators with varying concentrations and molecular weights of UV-PLCL (a), semiconductors (PLCL:P3HT, 8:2) (b), and conductors (HDD concentration, 10 %) (c), fabricated at different spin-coating speeds. (d) Thickness control of conductor films through multiple coating steps.

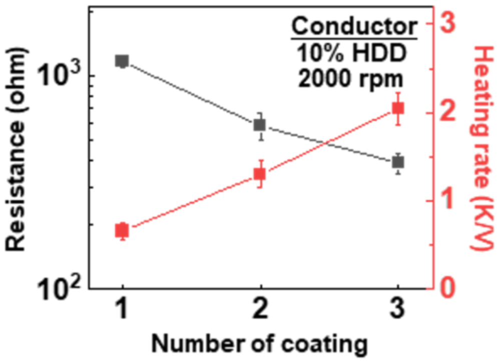

Figure S15. Variation in resistance and heating rate of a soft, stretchable, transient microheater as a function of coating number. Data are presented as mean values ± standard deviation. n=5 independent samples.

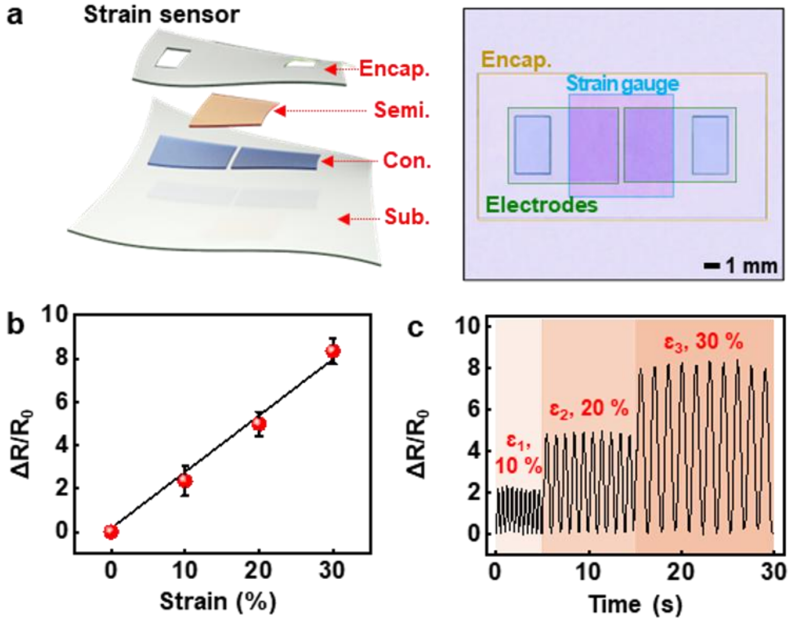

Figure S16. A stretchable, transient, strain sensor. (a) Schematic illustration (left) and optical micrograph (right) of a strain sensor. (b,c) Resistance changes of the strain sensor under uniaxial strains up to 30 % (b) and during cyclic loading of 10%, 20 %, and 30 % strains (c). Data are presented as mean values ± standard deviation. n=5 independent samples.

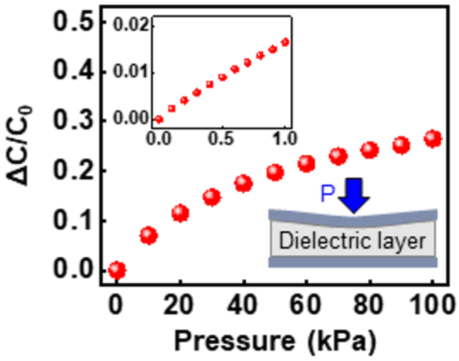

Figure S17. Pressure-dependent capacitance variation of a soft, stretchable, transient pressure sensor.

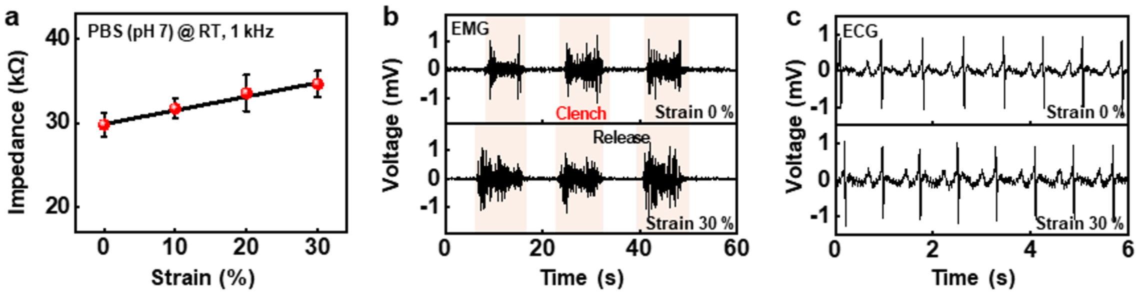

Figure S18. (a) Changes in impedance spectra under mechanical strain of 0–30 %. Data are presented as mean values ± standard deviation. n=5 independent samples. (b,c) Electromyography (EMG) (b) and electrocardiography (c) recordings acquired at the same strain conditions (0-30 %), demonstrating stable signal acquisition by the electrodes under mechanical deformation.

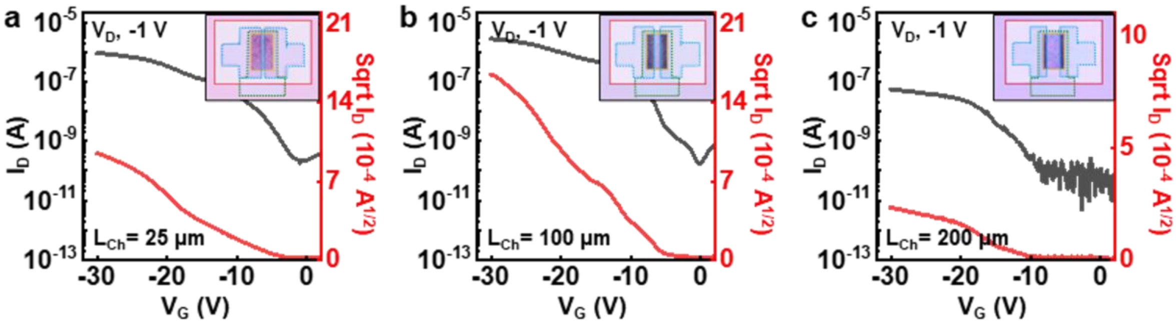

Figure S19. I-V characteristics of a soft, stretchable, transient OTFT with different channel lengths of (a) 25 μm, (b) 100 μm, and (c) 200 μm, and optical images of the corresponding devices in the insets.

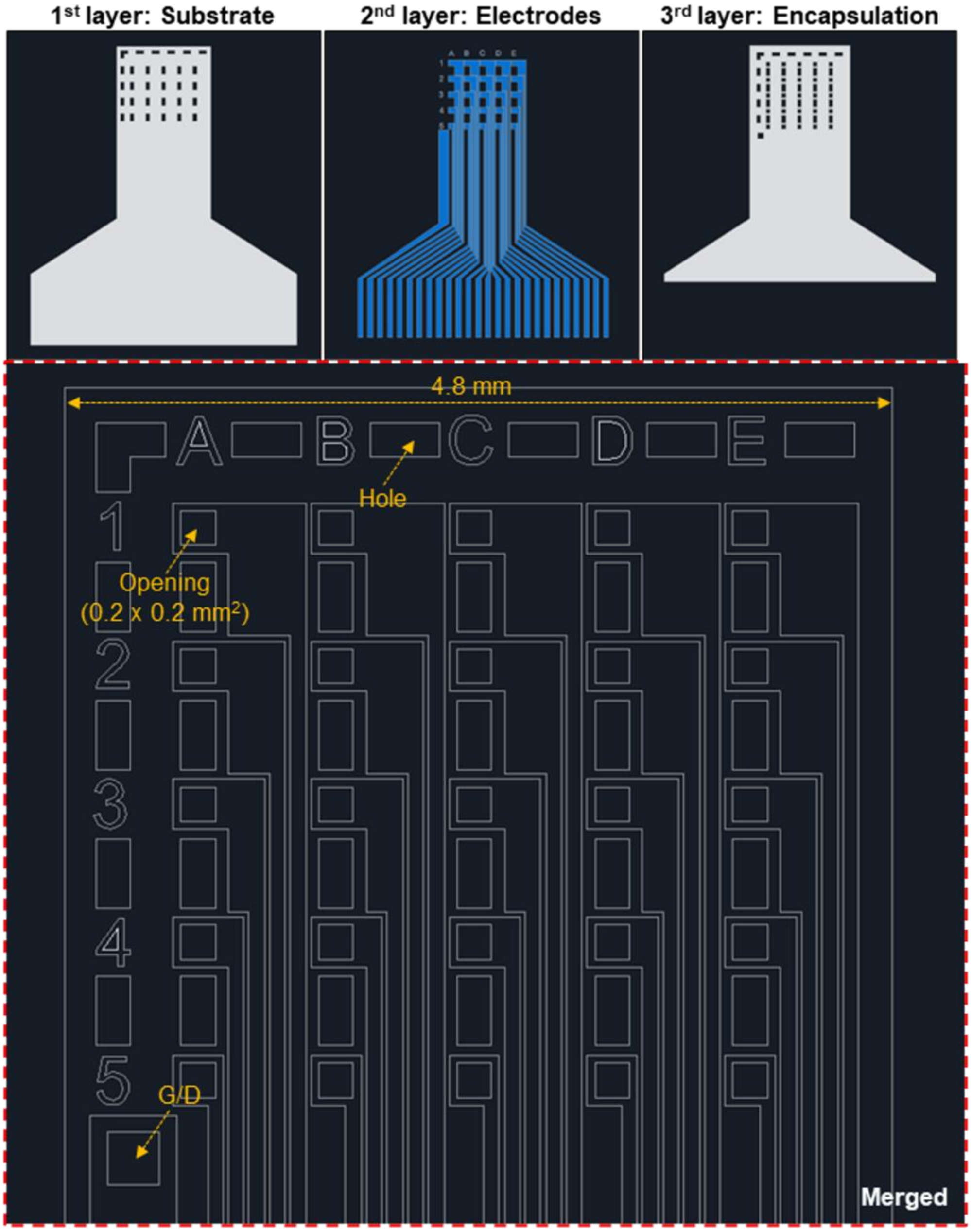

Figure S20. Device architecture of a soft, stretchable, transient epidural electronics (active area, 4.8 x 4.8 mm^2) featuring a 5 x 5 passive neural electrode array.

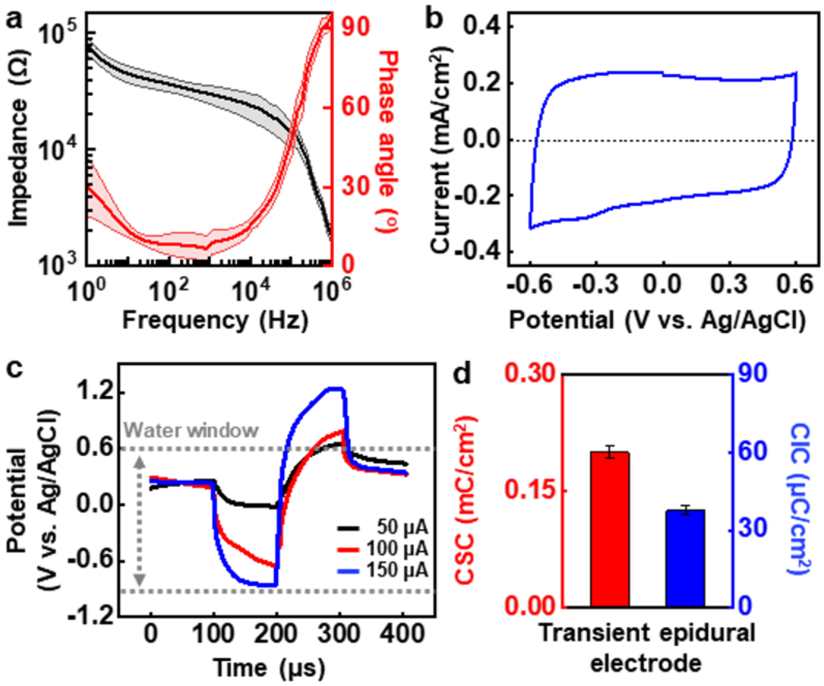

Figure S21. (a-c) Electrochemical impedance spectra (a), cyclic voltammetry (CV) curve from -0.6 V to 0.6 V, and voltage transient curves (c) of the transient epidural electrodes measured in PBS (pH 7), exhibiting an average impedance of ~30 kΩ at 1 kHz and charge storage capacity (CSC) and charge injection capacity (CIC) of ~0.2 mC/cm^2 and ~37.5 μC/cm^2, respectively (d). Data are presented as mean values ± standard deviation. n=5 independent samples.

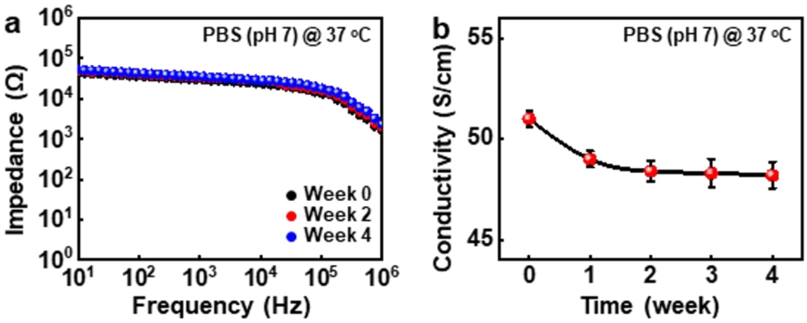

Figure S22. (a) Variations in electrochemical impedance spectra and (b) conductivity changes of the transient epidural electrodes in PBS (pH 7) at 37 °C over 4 weeks. Data are presented as mean values ± standard deviation. n=5 independent samples.

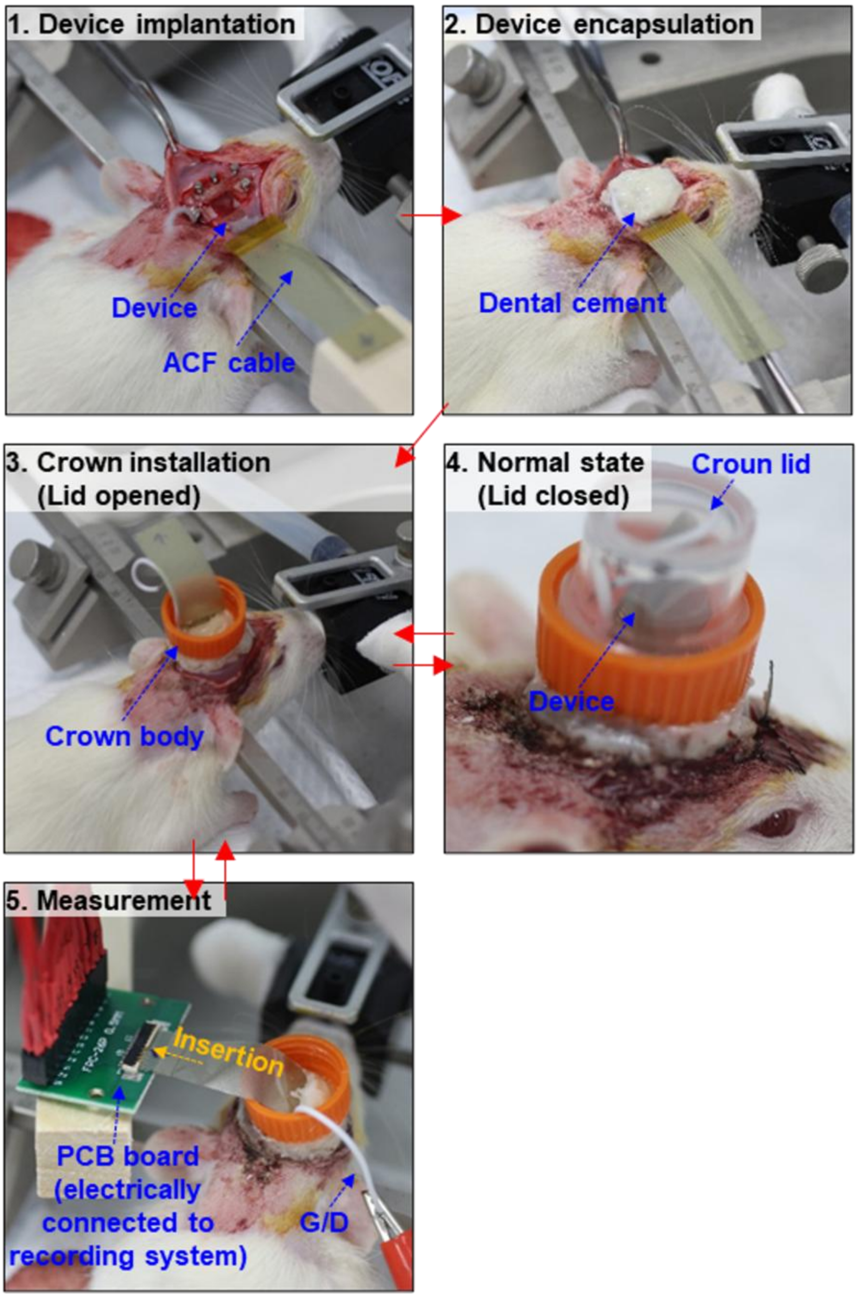

Figure S23. Photographs of the implantation process for the soft, stretchable, transient epidural electronics on the rat cortex.

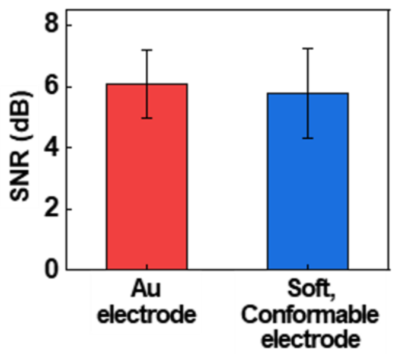

Figure S24. Comparative analysis of signal-to-noise ratio (SNR) of the Au and transient neural electrodes. Data are presented as mean values ± standard deviation. n=3 biologically independent animals per group.

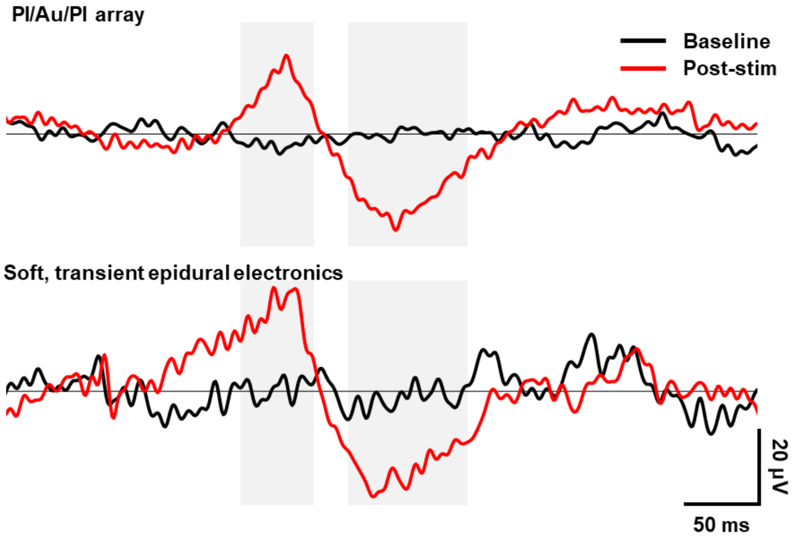

Figure S25. Comparison of ECoG signals recorded using a PI/Au/PI electrode array and the proposed transient epidural electrode array during the toe pinch test. Post-simulus signals (red) were compared to baseline signals (black), showing statistically significant differences between the two groups indicated by shaded regions (n = 10 biologically independent animals per group).

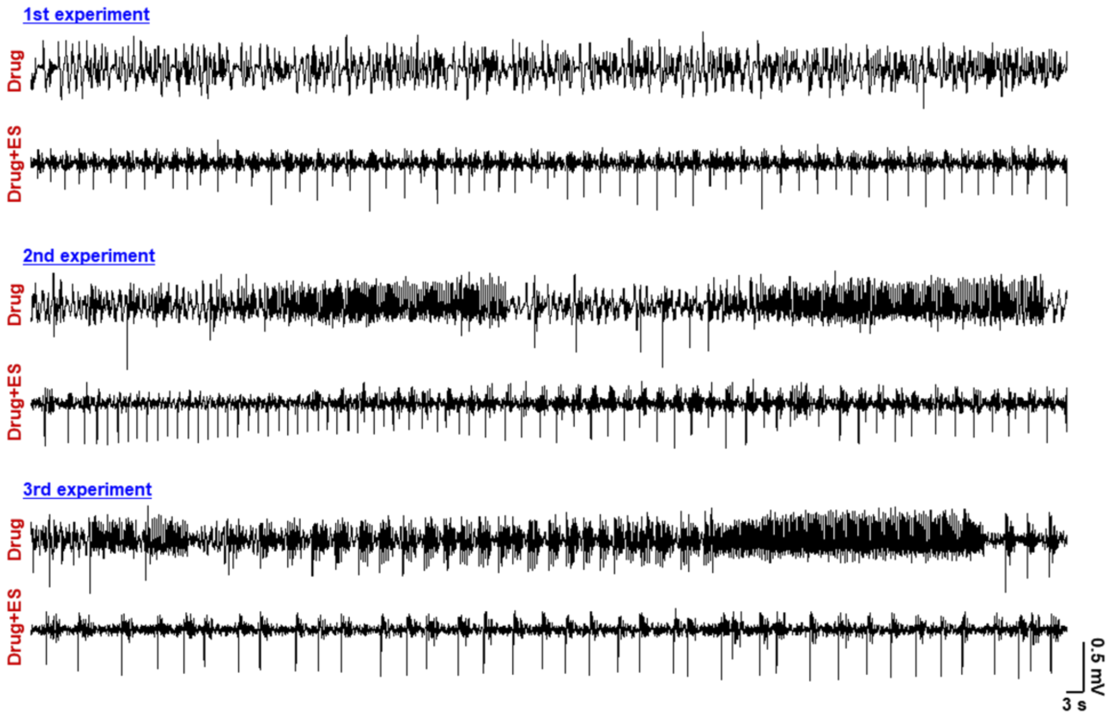

Figure S26. Repeated validation of seizure suppression by electrical stimulation using the transient epidural electrode array, where post-stimulation ECoG signals exhibited reduced spike frequency and amplitude compared to pre-stimulation recordings.

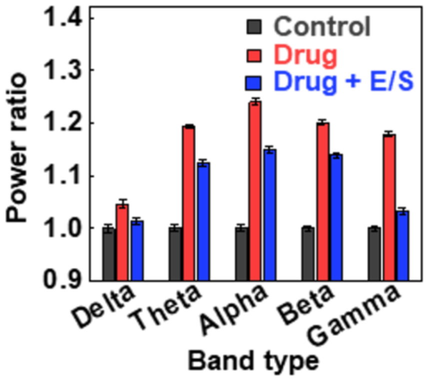

Figure S27. Power ratio comparison across ECoG frequency bands—delta (0.5-4 Hz), theta (4-8 Hz), alpha (8-13 Hz), beta (13-30 Hz), and gamma (>30 Hz)— before (Control), after drug administration (Drug), and after drug injection and electrical stimulation (Drug + E/S). The height of the boxes represents the mean power ratio relative to the control group. Data are presented as mean values ± standard deviation. n=3 biologically independent animals per group.

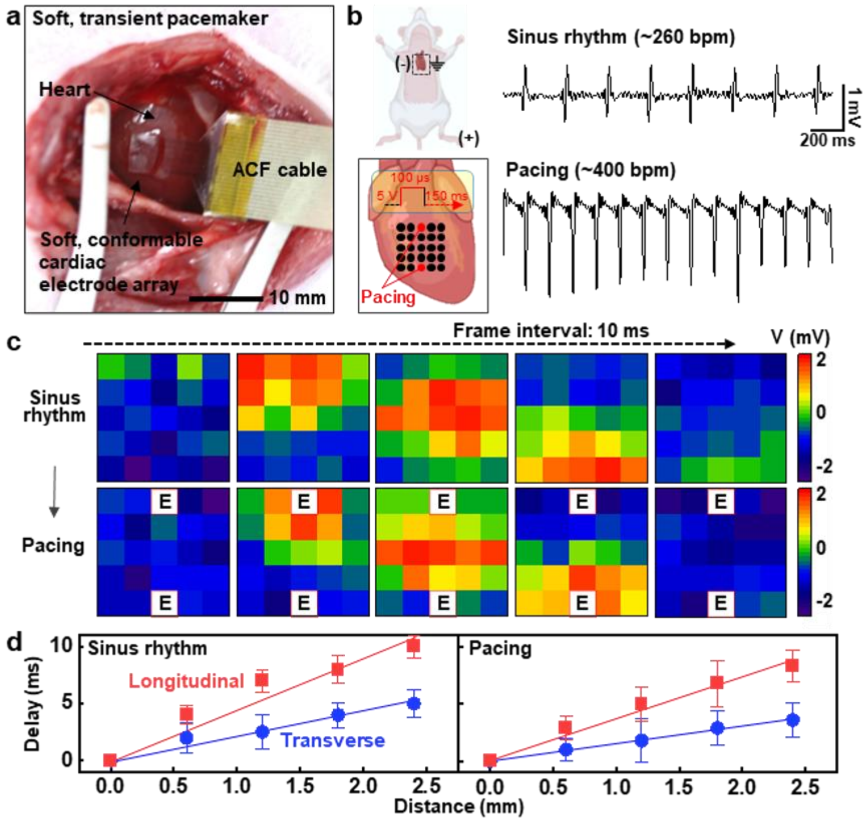

Figure S28. (a) Photograph of elastomeric, transient electrodes implanted onto a rat heart for epicardial ECG monitoring and cardiac pacing. (b) Schematic of the in vivo experimental setup for cardiac function modulation via electrical stimulation between two distant electrodes (left), and corresponding epicardial ECG recordings before and during pacing (right). (c) Spatiotemporal mapping of epicardial ECG biopotential patterns at five sequential time points with an interval of 10 ms. (d) Average longitudinal and transverse activation delays as a function of distance during sinus rhythm (left) and pacing (right), showing the pacing increased both longitudinal and transverse velocities from 0.24 m/s and 0.48 m/s to 0.29 m/s and 0.67 m/s [1-2]. Data are presented as mean values ± standard deviation. n=3 biologically independent animals per group.

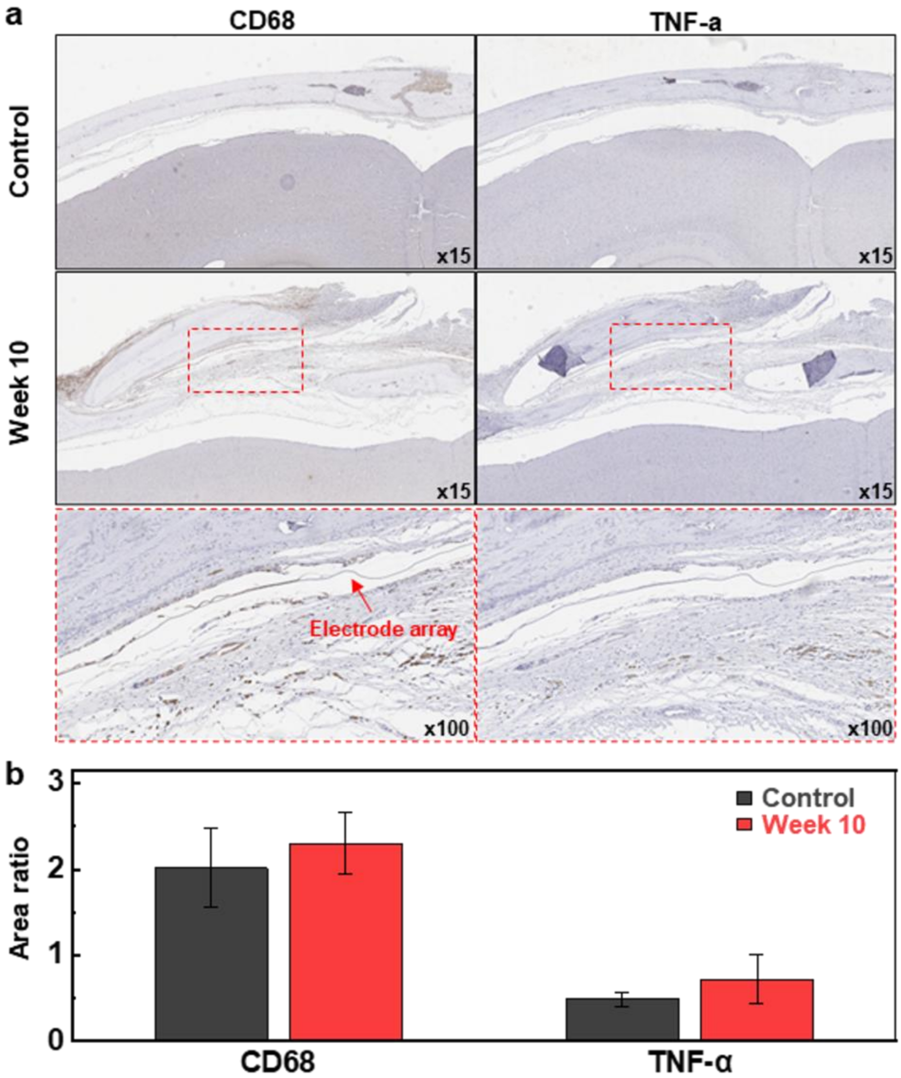

Figure S29. (a) Immunohistochemical stained images and (b) relative density quantification of CD68 and TNF-α in tissue sections before and after 10 weeks of device implantation. Data are presented as mean values ± standard deviation. n=3 biologically independent animals per group.

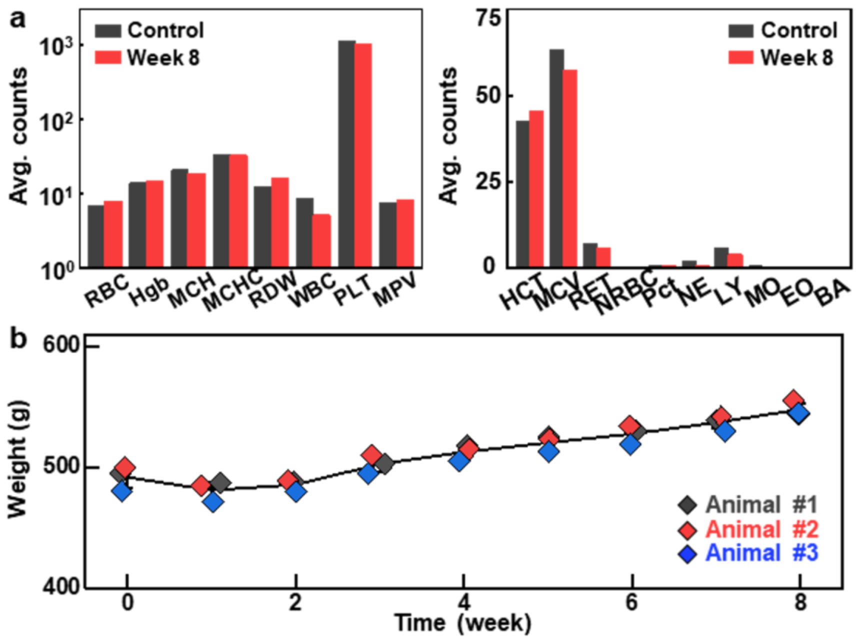

Figure S30. (a) Blood chemistry analysis of rats with and without device implantation for 8 weeks, indicating no significant physiological change. RBC, red blood cell, /μL; Hgb, hemoglobin, g/dL; MCH, mean corpuscular hemoglobin, pg; MCHC, mean corpuscular hemoglobin concentration, g/dL; RDW, red cell distribution width, %; WBC, white blood cell, /μL; PLT, platelet, /μL; MPV, mean platelet volume, fL; HCT, hematocrit, %; MCV, mean corpuscular volume, fL; RET, reticulocyte, %; NRBC, nucleated red blood cell, /μL; Pct, plateletcrit, %; NE, neutrophils, K/μL; LY, lymphocytes, K/μL; MO, monocytes, K/μL; EO, eosinophils, K/μL; BA, basophils, K/μL. (b) Body weight tracking of three animals during *in vivo* testing. Despite initial postoperative weight loss, continuous weight gain suggested healthy recovery.

Table S1. Comparison of processing cost and time between the traditional manufacturing approach and the proposed fabrication strategy for 4-inch soft, transient transistor arrays.

Traditional Manufacturing Process				This Work			
Steps	**Processes**	**Cost* ($)**	**Time** (h)**	**Steps**	**Processes**	**Cost* ($)**	**Time** (h)**
Sacrificial Layer	- Coating **PMMA** on a wafer - Coating **bottom PI**	2.5 - 4.4	1.5	Sacrificial Layer	- Coating **PAA** on a wafer	0.1 - 0.2	0.1
Channel	- Doping **silicon-on-insulator (SOI) wafer** - Wet etching of a box oxide - Transfer printing **Si NMs** onto PMMA/PI - **PR** patterning - Dry etching **Si NMs** - Removing **PR**	12.8 - 30.3 (SOI wafer: 200-700)	3	Substrate	- Coating **the insulator**	0.7 - 0.9	1
Source/Drain Electrodes	- **Mo** deposition - **PR** patterning - Wet etching **Mo** - Removing **PR**	5.3 - 10.3	4	Gate Electrode	- Coating **the conductor** - Photopatterning	2.4 - 3.2	0.5
Gate Dielectric	- **SiO_2** deposition - **PR** patterning - Wet etching **SiO_2** - Removing **PR**	4.3 - 7.3	4	Gate Dielectric	- Coating **the insulator** - Photopatterning	0.7 - 0.9	0.5
Gate Electrode	- **Mo** deposition - **PR** patterning - Wet etching **Mo** - Removing **PR**	5.3 - 10.3	4	Source/drain Electrodes	- Coating **the conductor** - Photopatterning	2.4 - 3.2	0.5
Finalizing	- Coating **top PI** - **PR** patterning - Dry etching **top PI** - Removing **PR**	6.6 - 11.8	1	Channel	- Coating **the semiconductor** - Photopatterning	0.5 - 0.7	0.5
	- Removing **PMMA** - Pick up - Dry etching **bottom PI** - Transfer printing onto **a biodegradable polymer sub.** - Dry etching **top PI**	6.6 - 13.2	2	Finalizing	- Removing **PAA** - Pick up	<0.1	1
Total		**243 - 787**	**19.5**	**Total**		**6.9 - 9.2**	**4.1**

* Price estimates are based on bulk prices from various vendors and include processing costs such as electricity and water usage.
** Coating time was approximated by considering coating, curing, and cooling steps;
Deposition and dry etching times were estimated by accounting for vacuum setup, process time, and cooling.

Table S2. Comprehensive comparison of recent transient (biodegradable) electronic devices in terms of materials, performance, fabrication processes, and applications.

Device	Materials	Performance	Fabrication	Scalability	Applications	Ref
Temperature sensor	Fe, Mo, SiO_2, Ge nanomembrane	~0.240 %/°C	Lithography, Deposition, Transfer printing	High	-	[3]
	Fibroin, PLA, MgO, Mg	~0.290 %/°C	Deposition	Low	-	[4]
	Galactomannan, Zn	~0.148 %/°C	Laser ablation, Transfer printing, Deposition	Low	Wearable temperature monitoring	[5]
	PLGA, Mg	~0.280 %/°C	Deposition, Lithography, Transfer printing	High	-	[6]
	Ecoflex, SiO_2, Si_3N_4, Mg	~0.245 %/°C	Dry etch, Transfer printing	High	Food/medical monitoring	[7]
	UV-PLCL, PEDOT:PSS/diacetylene	~0.254 %/°C	Solution process	High	-	This work
Strain sensor	PBAT, MgZnCa metallic glass	Gauge factor ~5	Deposition, Laser ablation	Medium	-	[8]
	PI, Mo, Si nanoribbon	Gauge factor ~0.2	Doping, Lithography, Dry etch, Transfer printing	High	Wearable motion detection, Cardiac monitoring	[9]
	Starch/Ti_3C_2Tx composite	Gauge factor ~36.2	Solution casting	Low	Wearable motion detection	[10]
	PEDOT:PSS/CNFs doped starch/NaCMC	Gauge factor ~3.9	Solution casting, Spray coating	Low	Human-machine interface	[11]
	UV-PLCL, PEDOT:PSS/diacetylene, PLCL/P3HT/diazirine	Gauge factor ~27	Solution process	High	-	This work
Pressure sensor	Cellulose, Carbon paste, Pectin xerogel	~0.029 /kPa (0–1 kPa)	Sintering, Carbonization, Sol-gel, Lamination	Low	Wearable motion detection	[12]
	Silk, Silver, Ecoflex	~0.0188 /kPa (0–4 kPa)	Electrospinning, Deposition, Lamination	Low	Wearable motion detection	[13]
	PVA, Zn, PLGA/PCL nanofiber	~0.888 /kPa (0–2 kPa)	Electrospinning, Deposition, Lamination	Low	Tactile sensor array	[14]
	PLA, Mg, PGS	~0.700 /kPa (0–1 kPa)	Solution casting, Lamination, Deposition, Lithography	Medium	Orthopaedic application	[15]
	UV-PLCL, PEDOT:PSS/diacetylene	~0.020 /kPa (0–1 kPa)	Solution process	High	-	This work
Transistor	SiO_2, Mg, MgO	660 cm^2/Vs mobility, ~10^5 on/off	Lithography, Dry etching, Transfer printing, Deposition	High	-	[16]
	Silk, PEDOT:PSS, PHB, C-dextran, C8-BTBT	4.22 cm^2/Vs mobility, ~10^5 on/off	Solution casting, Deposition	Medium	-	[17]
	PEDOT:PSS/Carbon nanofiber doped starch/cellulose	0.07 cm^2/Vs mobility, ~10^3 on/off	Solution casting, Inkjet printing, Deposition	Low	-	[18]
	UV-PLCL, PEDOT:PSS/diacetylene, PLCL/P3HT/diazirine	2.73 cm^2/Vs mobility, ~10^4 on/off	Solution process	High	-	This work
EP array	PLLA/PCL, Mo	10 kΩ @ 1 kHz (6 ch, 150 nm thick)	Solution casting, Dry etch, Deposition	Medium	ECoG monitoring	[19]
	PLGA, Mo	44 kΩ @ 1 kHz (16 ch, 100 nm thick)	Photo/soft lithography, Transfer printing	High	Cardiac monitoring	[20]
	PLGA, Polyanhydride, Mo	400 Ω @ 1 kHz (3 ch, 15 μm thick)	Laser ablation, Photocuring	Medium	Nerve regeneration	[21]
	SH-PLCL, PEDOT:PSS/PEG/ ionic liquid/glycerol, Mo	~100 Ω @ 1 kHz (2 ch, 2 μm thick)	Micro-molding, Transfer printing, Laser ablation/Medium	Low	Bladder monitoring	[22]
	UV-PLCL, PEDOT:PSS/diacetylene	30 kΩ @ 1 kHz (25 ch, 100 μm thick)	Solution process	High	Neural/cardiac monitoring	This work

References

1. Honarbakhsh, S., Roney, C., Horrach, C. V., Lambiase, P. D. & Hunter, R. J. Autonomic modulation impacts conduction velocity dynamics and wavefront propagation in the left atrium. *Europace* **26**, 1–12 (2024).

2. Wilhelm, T. I. *et al.* Influence of Heart Rate and Change in Wavefront Direction through Pacing on Conduction Velocity and Voltage Amplitude in a Porcine Model: A High-Density Mapping Study. *J. Pers. Med.* **14**, (2024).

3. Zhao, H. et al. Biodegradable germanium electronics for integrated biosensing of physiological signals. Npj Flex. Electron. 6, (2022).

4. Janus, K. A. et al. Transient magnesium-based thin-film temperature sensor on a flexible, bioabsorbable substrate for future medical applications. Applied Research 3, (2024).

5. Yi, N. et al. Fully water-soluble, high-performance transient sensors on a versatile galactomannan substrate derived from the endosperm. ACS Appl. Mater. Interfaces 10, 36664–36674 (2018).

6. Lee, S.-M. et al. Ecofriendly transfer printing for biodegradable electronics using adhesion controllable self-assembled monolayers. Adv. Funct. Mater. 34, (2024).

7. Salvatore, G. A. et al. Biodegradable and highly deformable temperature sensors for the internet of things. Adv. Funct. Mater. 27, 1702390 (2017).

8. Bae, J.-Y. et al. Biodegradable metallic glass for stretchable transient electronics. Adv. Sci. 8, 2004029 (2021).

9. Hu, B. et al. Ultrathin crystalline silicon-based omnidirectional strain gauges for implantable/wearable characterization of soft tissue biomechanics. Sci. Adv. 10,

eadp8804 (2024).

10. Dong, M. et al. Transient starch-based nanocomposites for sustainable electronics and multifunctional sensing. Adv. Funct. Mater. 35, (2025).

11. Vahdani, M. et al. Transient piezoresistive strain sensors based on elastic biopolymer thin films. ACS Appl. Polym. Mater. 6, 6530–6539 (2024).

12. Basarir, F. et al. Edible and biodegradable wearable capacitive pressure sensors: A paradigm shift toward sustainable electronics with bio-based materials. Adv. Funct. Mater. 34, (2024).

13. Hou, C. et al. A biodegradable and stretchable protein-based sensor as artificial electronic skin for human motion detection. Small 15, e1805084 (2019).

14. Khalid, M. A. U. et al. A highly sensitive biodegradable pressure sensor based on nanofibrous dielectric. Sens. Actuators A Phys. 294, 140–147 (2019).

15. Boutry, C. M. et al. A stretchable and biodegradable strain and pressure sensor for orthopaedic application. Nat. Electron. 1, 314–321 (2018).

16. Hwang, S.-W. et al. A physically transient form of silicon electronics. Science 337, 1640–1644 (2012).

17. Yang, Y. et al. High-mobility fungus-triggered biodegradable ultraflexible organic transistors. Adv. Sci. 9, e2105125 (2022).

18. Viola, F. A. et al. All-organic transistors printed on a biodegradable and bioderived substrate for sustainable bioelectronics. Mater. Today Bio 29, 101274 (2024).

19. Xu, K. et al. Bioresorbable electrode array for electrophysiological and pressure signal recording in the brain. Adv. Healthc. Mater. 8, e1801649 (2019).

20. Chen, Z. et al. Soft, bioresorbable, transparent microelectrode arrays for multimodal spatiotemporal mapping and modulation of cardiac physiology. Sci. Adv. 9, eadi0757 (2023).

21. Lee, G. et al. A bioresorbable peripheral nerve stimulator for electronic pain block. Sci. Adv. 8, eabp9169 (2022).

22. Jang, T.-M. et al. Stretchable and biodegradable self-healing conductors for multifunctional electronics. Sci. Adv. 10, eadp9818 (2024).